
Please note that this is a preprint listed on EarthArXiv which has not undergone full peer review yet. Subsequent versions may have slightly different content. If accepted, the final version of this manuscript will be available via the ‘Peer-reviewed Publication DOI’ link on the right-hand side of this webpage. Please feel free to contact any of the authors; we welcome the feedback.

1 **Sensitivity, Accuracy and Limits of the Lightweight**
2 **Three-Component SmartSolo Geophone Sensor (5 Hz)**
3 **for Seismological Applications**

4 **Martin Zecka¹, Koen Van Noten¹, Thomas Lecocq¹**

5 ¹Royal Observatory of Belgium, Avenue Circulaire 3, 1180 Brussels, Belgium

6 **Key Points:**

- 7 • instrument tests
8 • nodal systems
9 • SmartSolo
10 • sensor performance

Corresponding author: M. Zeckra, martin.zeckra@seismology.be

Abstract

[enter your Abstract here]

Introduction

Recent developments in seismological research have seen tremendous increases in sheer size of data throughout the last decade (Quinteros et al., 2021; Arrowsmith et al., 2022). This evolution has been accompanied by increasing computational power enabling the processing of such large data-sets (Ahrens et al., 2011; Bozdog et al., 2014; MacCarthy et al., 2020) and the introduction of Machine Learning techniques for seismological data processing (Bergen et al., 2019; Kong et al., 2019; Arrowsmith et al., 2022). On the hardware side, the introduction of low-cost geophone sensors (e.g., Raspberry Shake) often in combination with wholistic software/hardware solutions enabled data recording in unprecedented quantity of stations and for non-scientific audiences, for which the term "citizen science" has been introduced (Chen et al., 2020; Subedi et al., 2020; De Plaen et al., 2021; Calais et al., 2022). While the use of such low-cost instrument is limited and cannot cover the full range of seismological methods (Anthony et al., 2019), integrated nodal systems bear the potential to present a cost-efficient compromise of the performance in between citizen instruments and classical seismological sensors.

Nodal systems are common practice in active seismic experiments for exploration of hydrocarbon and other resources (Dean et al., 2018), in which numerous geophones (mostly single component instruments) are regularly spaced over a site of interest recording subsurface reflections of actively induced signals (e.g., explosive or sweep). Besides extending to three-component instruments, latest developments in geophone sensors for nodal installations saw major efforts in enhancing the level of autarky. To overcome issues of power supply, communication and time accuracy in remote locations, integrated nodal systems eliminate cable-based solutions and incorporate digitizer, data storage, GPS and battery in a single acquisition unit (Dean & Sweeney, 2019). The first commercially available node that also enabled continuous data recording was the Fairfield ZLand node (A. T. Ringler et al., 2018). This instrument is also eligible to be used for seismological research questions. With a fraction of the purchasing costs compared to standard seismological acquisition systems, the installation of so-called Large N arrays with 100s to 1000s of nodes became possible (Hand, 2014; Karplus & Schmandt, 2018; Roux et al., 2018; Brenguier et al., 2015). One of the first installations of such kind was

43 realized in the Los Angeles basin with $\sim 13,000$ seismic stations covering an area of 16
 44 x 16 km with three separated arrays and equidistant sensor spacing of 100m that enabled
 45 unprecedented spatial sampling of wavefield and site-characteristics (Castellanos & Clay-
 46 ton, 2021).

47 SmartSolo[®] recently (ADD DATE?, @Thomas 2018??) released their IGU-16 se-
 48 ries instruments. These geophone instruments with a 5 Hz natural frequency are avail-
 49 able as single (IGU-16 1C) or three-component (IGU16-HR 3C) sensors and are equipped
 50 with 24 bits digitizers and GPS. Batteries are modular and available as High Capacity
 51 Battery or Standard Capacity Battery Packs which, together with the sensor, eventu-
 52 ally provides a single, closed casing sensor. The total weight of the 3C (2.4 kg high ca-
 53 pacity, 1.7 kg standard capacity battery) and size (10.3 x 9.5 x 18.7 cm) outperforms clas-
 54 sical seismometer-digitizer set-ups. During the installation of larger surveys, the oper-
 55 ator profits from the reduced man-power and time necessary. Due to the modular de-
 56 sign of the nodes that allows the replacement of their spike base with a tripod battery
 57 base, these sensors' potential use becomes independent from the available surface struc-
 58 ture in the survey area, i.e., urban environments with a high degree of sealing. In the
 59 last years, the SmartSolo node series have been increasingly used for Large N installa-
 60 tions in the field of passive seismology (e.g. Obermann et al., 2022; Chmiel et al., 2019).

61 So far, a comprehensive study identifying the capabilities of geophone-based node
 62 sensors for seismological purposes has only been performed for the Fairfield ZLand sen-
 63 sors (A. T. Ringler et al., 2018), but is yet unavailable for the SmartSolo sensors. In this
 64 study we evaluate the SmartSolo instruments characteristics, performance and limits in
 65 order to justify their use in a variety of seismological applications. In a set of lab-based
 66 experiments we identify the sensors' transfer function, control the manufacturer's given
 67 poles and zeros, check the self-noise level, and compare the sensors with well-calibrated
 68 seismometers. After that, we show the performance of the sensors during field installa-
 69 tions with two examples focusing on teleseismic waveforms and ambient seismic noise
 70 measurements.

Instrument tests

Instrument response derived from coherent waveforms

In the recording of ground shaking, a seismic sensor acts as a filter in the sense of a linear, time-invariant system (LTI) (Scherbaum, 2006) when translating it into electric voltages as an output signal. This alternation from input to output signal is represented through the system's frequency response function or the transfer function. The quantitative description of the LTI then allows us to restore the original input signal by applying signal restitution to the obtained waveforms without further knowledge of the physical processes going on inside the filter (Scherbaum, 2006). The transfer function is then characterized by the complex poles and zeros.

Havskov & Alguacil (2015) have shown that it is possible to estimate the transfer function of a seismometer by using the natural vibrations of the ground as a shaking table recorded with two closely installed sensors. For the SmartSolo sensors, the output signal is expected to be contaminated by instrument noise and thus, we applied the cross-spectrum method (Eq. 1). In this method, the output of seismometer 1 is the input of seismometer 2 as a linear system that presents a transfer function in the form of:

$$T_2(\omega) = T_1(\omega) \frac{P_{21}(\omega)}{P_{11}(\omega)} \quad (1)$$

with P_{21} as the cross-spectrum between the outputs of both sensors and P_{11} as the autpower spectrum of the output of sensor 1. Under the assumption the instrument response (as poles and zeros) given by the manufacturer is correct for sensor 1, we can estimate the unknown response of sensor 2. This is repeated for all instrument pairs.

The estimation of the instrument response parameters represented by its poles and zeros is a non-linear operation. Therefore, T_2 is identified through the optimization of the poles and zeros and fitting the theoretical response function to the observed transfer function presented in equation 1. The misfit function of the optimization is represented by the complex L2-norm.

In order to obtain highly correlated ground motions, 24 3C nodes have been closely co-located (in a so called 'huddle', Fig. 1c) in a regular grid of 1m x 1m overall extension close to the Uccle permanent station of the Belgian seismic network (international

99 code BE.UCC, Royal Observatory of Belgium, 1985). The location within Brussels as-
 100 sured a high noise level. During the recording period a teleseismic earthquake could be
 101 recorded (M7.3, Japan, GEOFON Data Centre, 1993) that further guarantees strong cor-
 102 relation of the obtained wavefield.

103 The resulting poles for the instrument response estimation strongly converge to-
 104 wards the values given by the manufacturer ($-22.2111-22.2178i$, $-22.2111+22.2178i$),
 105 with half of the estimated transfer functions obtaining misfits below 5%. The weighted
 106 mean for poles below this misfit threshold differs by $-0.0559\mp 0.0552i$ from the man-
 107 ufacturer given values. Considering only the results with misfits below 2%, the poles dif-
 108 fer by $-0.0162\mp 0.0158i$. Stronger misfit of the resulting transfer functions are foremost
 109 proportional to intersensor distances as the higher frequency sections of the recorded noise
 110 spectra de-correlate with increasing distance. This result could be reproduced for the
 111 horizontal components as well, with an overall greater spread of high misfit poles and
 112 zeros. This is likely due to the higher self-noise of the horizontal components (section
 113 2.2) that leads to less coherent waveforms, as they show lower signal-to-noise ratio of the
 114 teleseismic phases and are more affected by tilt of the sensor that reduces the overall sen-
 115 sitivity. However, the limitation to results with misfits below 5% or 2% leads to the same
 116 range of differences between manufacturer and estimated poles and zeros as determined
 117 for the vertical component.

poles	$-22.2111 - 22.2178i$	$-22.2111 + 22.2178i$
zeros	$0i$	$0i$
sensitivity (@0 gain)		$76.7e3 \frac{mV}{m/s}$
digitizer gain		3355.4432

Table 1. Instrument Response for a SmartSolo IGU-16HR-3C node represented by Poles and Zeros.

118 Instrument self-noise and long-term noise stability

119 The experiment set-up presented in figure 1c of 24 co-located SmartSolo 3C instru-
 120 ments allowed us to apply the three instrument approach of Sleeman et al. (2006) to iden-
 121 tify the instrument’s self noise based on a common, coherent input data. Here, we rely

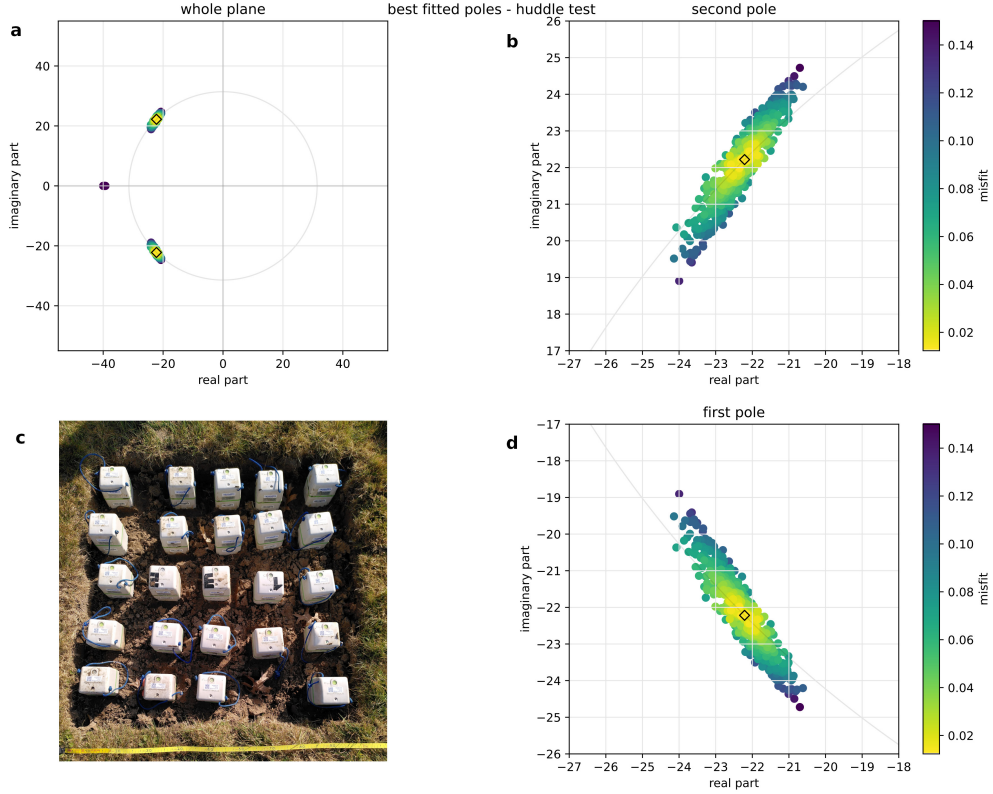


Figure 1. The resulting poles of the SmartSolo nodes huddle test, color-coded by misfit from the manufacturer’s values, shown by the diamond marker. a) result shown over the whole complex plane that has been defined as the solution space in the inversion. b) and d) close-up view of the two poles. c) 24 nodes co-located during the huddle test. Note the slightly imperfect installation, contributing negatively to the misfit values.

122 on the analysis of actual ground motion recordings during the self-noise test. As the sen-
 123 sor and digitizer are located within the same casing, we cannot measure their self-noise
 124 independently and the full recording system combining both sensor and digitizer is an-
 125 alyzed. For the most part, the self noise of digitizers lies up to 20dB below the self noise
 126 of the sensors A. T. Ringler et al. (2014) and thus we assume that the obtained noise
 127 spectra will reflect only the sensor’s self noise.

128 The comparison was performed for each instrument (i) using the two closest neigh-
 129 boring sensors of the grid (j, k). Similar to the huddle test, the use of the cross-spectrum
 130 (P_{ji}, P_{ik} , etc.) between the sensors eliminates the sensor’s transfer functions and noise
 131 cross-spectra. The systems self-noise autospectrum (N_{ii}) then can be expressed solely

132 through power- and cross-spectra of the obtained output of the three sensors (i, j, k)
 133 under the assumption of a common recording input as follows:

$$N_{ii} = P_{ii} - P_{ji} \cdot \frac{P_{ik}}{P_{jk}} \quad (2)$$

134 In order to retain comparability of the experiment outcome of A. T. Ringler et al.
 135 (2018) in which the authors performed a lab test for the Fairfield nodes on a shaking ta-
 136 ble and comparison with broadband sensors, we apply the same Fourier transformation
 137 parameters, prior downsampling (decimate from 250 to 50 Hz), and moving average to
 138 smooth the resulting spectra. The input data is a 1-hr period at a Thursday night (2022-
 139 03-17 01:30:00 UTC) in order to minimize the environmental noise close to the BE.UCCS
 140 station (lat 50.797, lon 4.36) in an open field as the spike at the bases could not be re-
 141 moved. In order to reduce errors propagating from transfer functions uncertainties, the
 142 input waveforms have been restituted (A. Ringler et al., 2011).

143 The resulting self-noise is stable between 0.7 to 15 Hz at around -160 dB (figure
 144 2), just above the global lower noise model (NLNM, Peterson, 1993). For lower frequen-
 145 cies the self-noise is steadily increasing but remains below the NLNM until 0.2 Hz. For
 146 higher frequencies the self-noise is decreasing and shows stronger instabilities in the spec-
 147 tral amplitudes. The overall shape of the noise spectrum is comparable to the Fairfield
 148 nodes (A. T. Ringler et al., 2018), while for the frequency range < 2 Hz the SmartSolo
 149 node outperforms the Fairfield sensor. This observation underlines the good sensitivity
 150 of the SmartSolo nodes for a seismological purpose as a passive sensor for temporal in-
 151 stallations for recording ambient seismic noise, detecting local tectonic and/or induced
 152 earthquakes, investigating activity in geothermal fields, and they remain performant over
 153 a large frequency range from 5 s to their chosen Nyquist frequency (here 25 Hz). The
 154 increase in noise level towards the higher periods probably makes them less suitable to
 155 investigate teleseisms, microseism and storms.

156 The horizontal components show on average a 15 dB higher noise level that are more
 157 sensitive to signal distortion due to tilt. The cross- sensor comparison of all 24 installed
 158 instruments in the Huddle test experiment shows no major distortions or anomalies for
 159 individual instruments. Only a stronger variability of the noise spectra at higher frequen-
 160 cies above 5 Hz can be observed. We suggest this might be related to the different level
 161 of coupling of each sensor that further introduces incoherencies in the recorded wave-

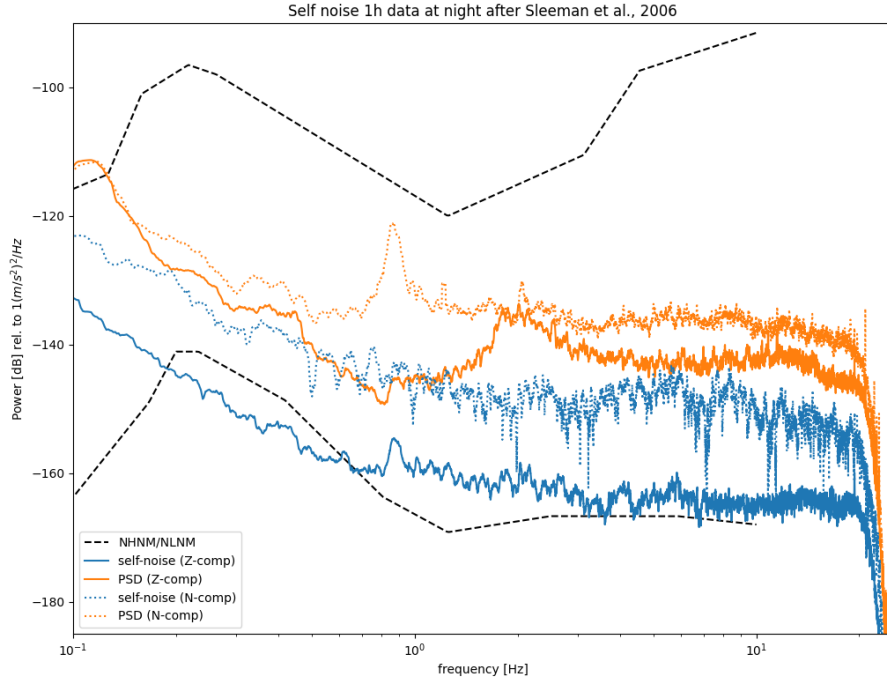


Figure 2. Outcome of the self-noise test following Sleeman et al. (2006). Blue curve is the estimated system self noise for a SmartSolo 3C sensor (vertical component). Orange curve shows the power spectrum of the recorded ground motion. The dashed colored lines show the equivalent for the North component. The black, dashed lines give the upper and lower global noise model bounds (Peterson, 1993).

162 fields in the ambient noise frequency range. Such incoherence of the input of the three
 163 sensors is then further propagated into the noise spectrum analysis. In future analyses
 164 of the SmartSolo sensors this could be avoided by using a shaking table instead of re-
 165 lying on coherent waveform recordings. The three first generation instruments (indicated
 166 in figure 1c with the letters 1, 2, 3) installed alongside the newest generations show the
 167 same outcome.

168 Comparison with well-calibrated seismometers

169 In a lab-based instrument test, the SmartSolo sensors were compared with well-
 170 calibrated, standard seismometers. The SmartSolo nodes were co-located with (*i*) the
 171 surface sensor of the Uccle station (network station code: BE.UCCS), that consists of

	Güralp DM24 + 3ESP	CityShark II + Lennartz 3D	SmartSolo
natural/corner frequency	30 s	5s	5 Hz
sampling frequency	100 Hz	250 Hz	250 Hz
downsampled frequency	50 Hz	50 Hz	50 Hz

Table 2. Overview of seismometer and digitizer combinations with sampling specifications.

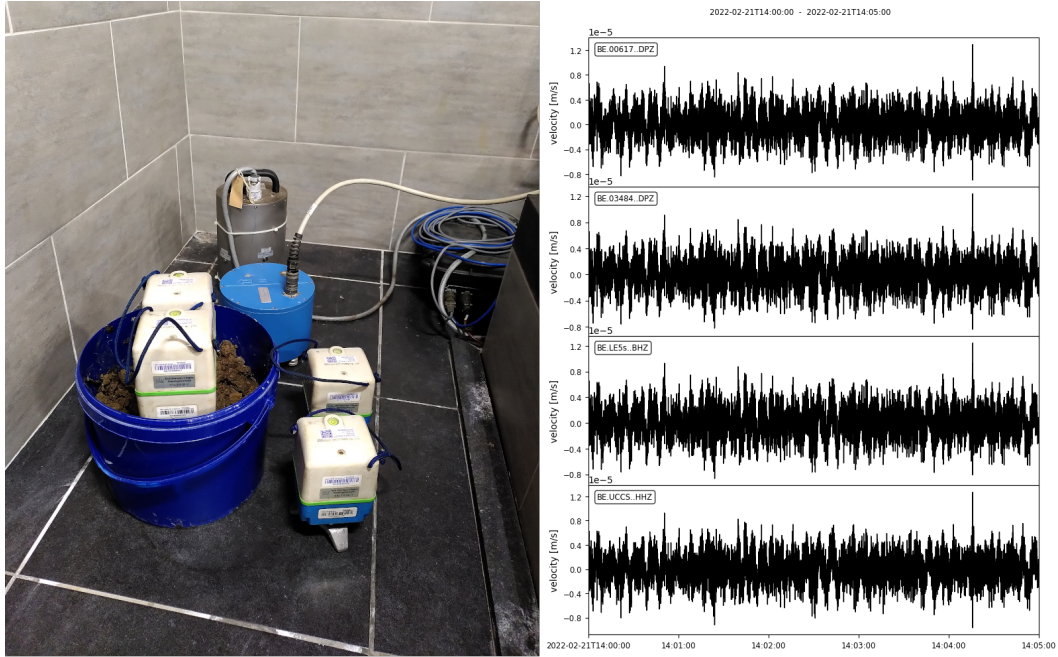


Figure 3. Co-location test of Smartsolo sensors with well-calibrated seismometers. Left: Two nodes each with different base set-ups either on a tripod or with a central spike in a sand-filled bucket, Lennartz LE3D/5s (blue instrument) connect to a Cityshark and Uccle surface station BE.UCCS (gray instrument in the back, Güralp CMG 3ESP). Right: restituted waveforms of all four kinds of sensors: From top to bottom: 1) node in bucket, 2) node on tripod, 3) LE3D/5s, 4) permanent sensor.

172 a Güralp DM24/3ESP instrument, and (*ii*) with a Lennartz 3D sensor connected to a
 173 CityShark digitizer (Chatelain et al., 2000) for comparison to a standard instrument that
 174 is used for ambient seismic noise measurements (figure 3). During this experiment, we
 175 also investigated if the modular use of different base set-ups of the Smartsolo nodes al-
 176 ters the recorded noise field. Two different set-ups were tested: (*i*) a 3C node connected
 177 to the High Capacity Battery Pack (gray) on a central spike installed in a sand-filled bucket

178 and (ii) a 3C node connected to the Standard Battery Pack (blue) on a steel tripod base
 179 installed on the floor of the cave next to the listed seismometers above (figure 3).

180 To compare the obtained waveforms in the time and spectral domain, we first re-
 181 moved the instrument responses of all sensors (table 1). The restituted waveforms of all
 182 four sensor types are highly congruent in obtained ground velocity amplitudes and time
 183 accuracy. This congruence demonstrates the accuracy of the nodes' poles and zeros iden-
 184 tified during the huddle test (see section above). In order to quantify the waveform sim-
 185 ilarity, we computed the coherence of all instrument combinations as the normalized cross-
 186 spectra (figure 4).

187 In comparison to the well-calibrated Gralp instrument, the node sensor installed
 188 on a tripod has the highest overall coherence with nearly perfect similarity from 20 Hz
 189 down to 10 s, way below its natural frequency (figure 4). A small deviation is present
 190 between 0.85 and 1.05 Hz that is more evident for the nodes with a central spike, but
 191 the waveform similarity always exceeds a 0.9 coherence. The decreasing coherence above
 192 20 Hz for the SmartSolo sensors appears to be a filter artifact that propagates from the
 193 different decimation applied to the waveforms to result in a common sampling frequency
 194 (table 2). For the CityShark with Lennartz instrument the ~ 1 Hz coherence drop is
 195 absent but above 4 Hz the waveform similarity to all other sensors in this test is steadily
 196 decreasing and falls below 0.9 at around 13 Hz. Due to the absence of a lowpass filter
 197 close to the Nyquist frequency of the raw data, we presume the existence of an analog
 198 filter in the CityShark digitizer with a cut-off that starts around 13 Hz and is not included
 199 in the instrument's transfer function.

200 The instrument comparison in the spectral domain is visualized in figure 4 and was
 201 obtained by dividing the power spectra of all instruments with all other instruments co-
 202 located during the experiment. Similar to the waveform similarity, we obtain flat spec-
 203 tral divisions at the ratio of 1 from $\lesssim 10$ Hz down to less than 10s. Here, the similarity
 204 deviation around ~ 1 Hz of the SmartSolo sensors becomes evident again and also is
 205 more pronounced for the sensors with a central spike installed in a sand-filled bucket.
 206 However, this effect can only be observed for the vertical components and is absent for
 207 the horizontal components. In the low frequency range below 0.2 Hz (remind that the
 208 node's natural frequency is 5 Hz) the horizontal spectra of the SmartSolo sensors devi-
 209 ate stronger from the spectrum obtained with the well-calibrated instrument as it can

210 be observed for the vertical components. The deviation from the well-calibrated instru-
 211 ment is even larger for sensors that were installed with a spike in the sand-filled bucket
 212 and thus, results from the fact that the nodes were not fully buried and resulting in poorer
 213 leveling in comparison to the tripod based nodes.

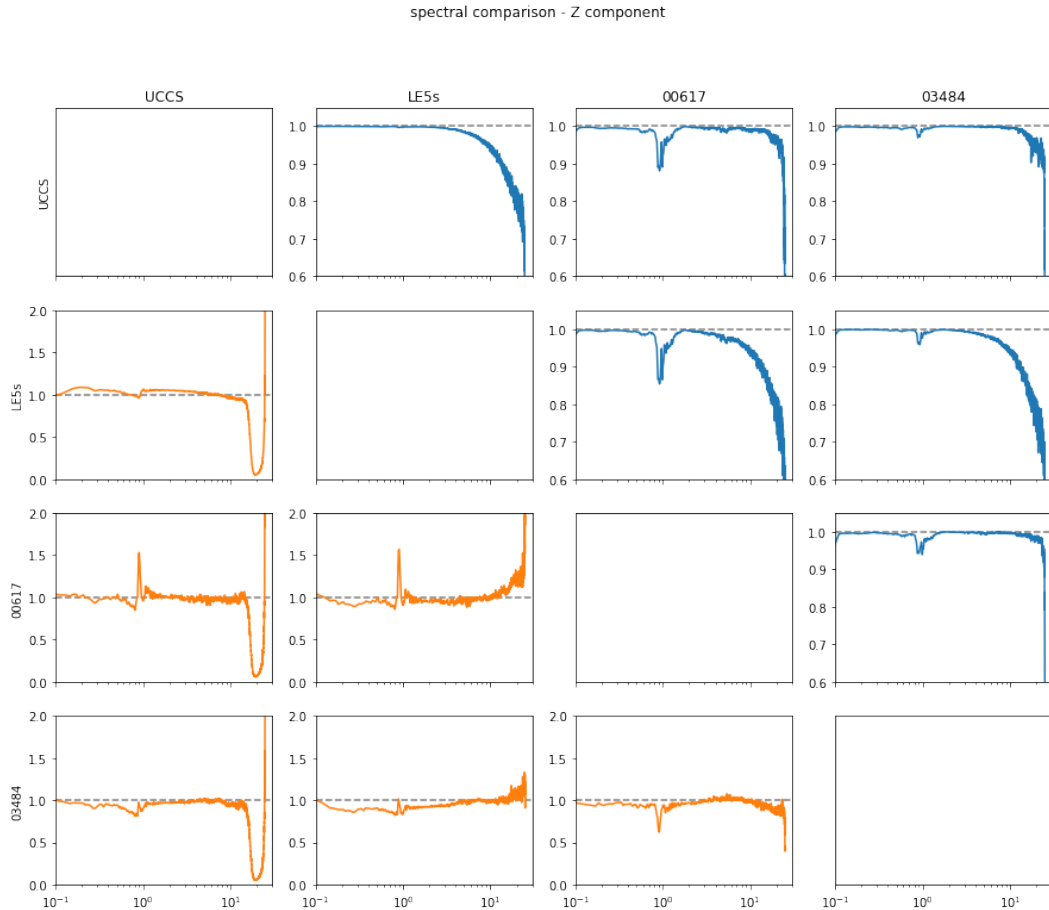


Figure 4. Waveform similarity between different types of sensors. Upper part (blue curves) shows the coherence amplitudes between the different sensors. Lower part (orange curves) gives the spectral divisions of all sensor combinations.

214 Real-world observations (applications, sensitivity)

215 Teleseismic arrivals

216 In the previous chapter, it was shown that the waveforms obtained with the Smart-
 217 Solo nodes bear the potential to recover ground motion far below their own natural fre-
 218 quency. During two longer term SmartSolo array installations in 2020 and 2022 around

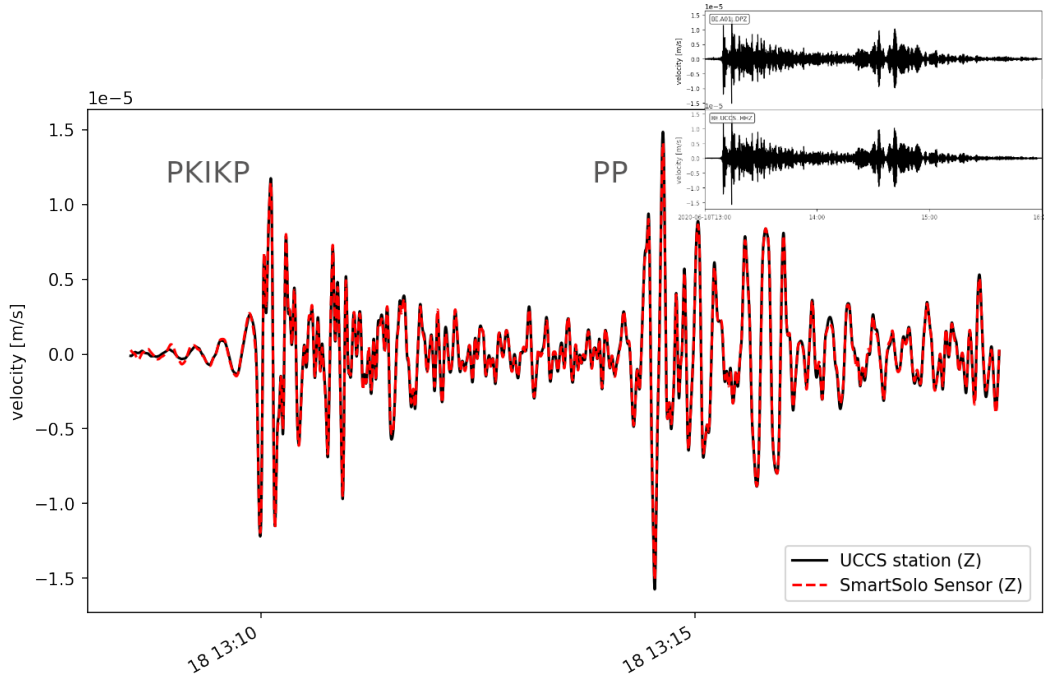


Figure 5. Teleseismic PKIKP and PP phases of the Mw 7.4 Kermadec earthquake (June 18, 2020) recorded with the vertical components at the BE.UCCS station (black) and with a single Smartsolo sensor (red). Both waveforms have been restituted to velocity and filtered between 20 s and 3 s. The inlet shows the full length (3 hours) of the teleseismic earthquake recorded with the SmartSolo Node (top trace) and the Güralp sensor (lower trace).

219 the BE.UCCS station, two teleseismic events in Kermadec (Mw 7.4, June 18, 2020) and
 220 Japan (Mw 7.3, March 16, 2022) respectively occurred during the surveys. To compare
 221 the node's performance with BE.UCCS, waveforms were first restituted to velocity and
 222 then bandpass filtered between 20 s and 3 s (figure 5).

223 The waveforms of the vertical component of a single Smartsolo sensor perfectly match
 224 the waveforms obtained with a Güralp instrument, with only slightly higher amplitudes
 225 for BE.UCCS. For both waveforms, the first arrivals of the body wave phases could be
 226 identified on a single vertical component for both events (PKIKP for Kermadec at 162°
 227 degree distance and PP for Japan at 84° distance). The surface waves of the 2022 Mw
 228 7.3 Japan earthquake could only be retrieved when lowering the bandpass filter down
 229 to 100 s, due to their lower dominant frequencies.

230 The horizontal components have a much reduced sensitivity in the very long pe-
 231 riod range. Thus for the Mw 7.4 Kermadec event, the earthquake can only be identified
 232 by stacking the waveforms of at least 20 nodes. It is important to mention that the sta-
 233 tion BE.UCCS around which the tests were performed is located in the city of Brussels
 234 and possesses one of the highest seismic noise levels in the whole BE network (Lecocq
 235 et al., 2020). In contrast, for the Mw 7.3 Japan earthquake, the first arrival S-phases and
 236 the surface waves can already be identified on a single horizontal sensor, but at the same
 237 cost as described before for the vertical component.

238 Ambient noise application

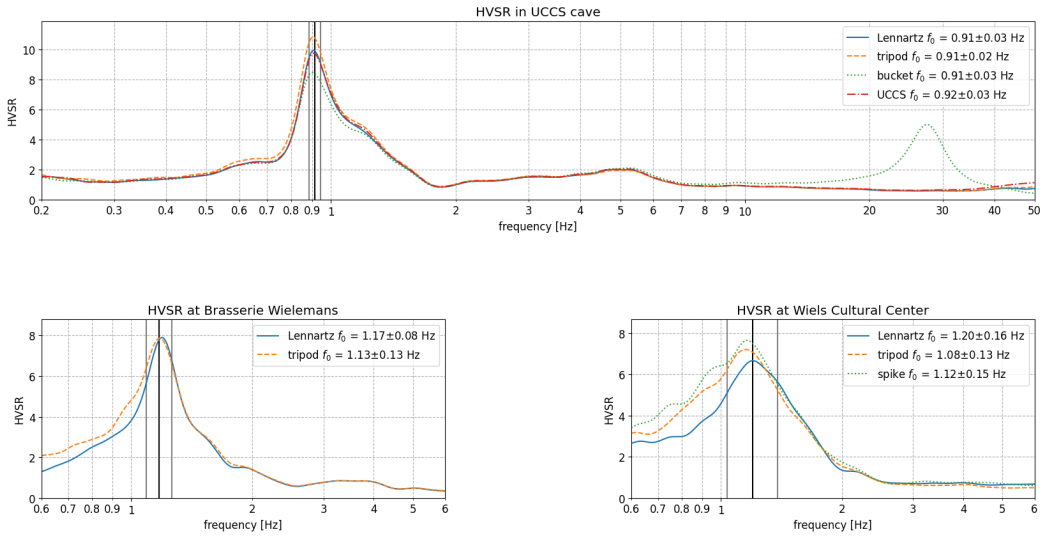


Figure 6. Instrument comparison through H/V analysis at three locations in Brussels. Waveforms have been restituted before the processing. HVSr graph from recordings a) at the location of UCC surface sensor (50.7973N, 4.3605E) from the sensor comparison lab test (fig. 3), with the blue solid line for LE3D-5s with Cityshark, orange dashed line for SmartSolo node on tripod base, green dotted line for node with spike in a sandfilled bucket and red dot-dashed line for Guralp permanent sensor. b) Location of the former Wielemans Brewery (50.8261N, 4.32646E) with LE3D-5s and Smartsolo sensors ~ 10 cm apart. c) Location at the Wiels Cultural Center (50.82453N, 4.3259E) with LE3D-5s, node on tripod and node with spike dugged into a grass field. Intersensor distance 5 - 10 m.

239 The preceding lab-based tests infer a suitable frequency range that justifies to use
 240 the SmartSolo sensors for passive measurements of ambient seismic noise in the frequency

241 range of 0.2 to 25 Hz. As an example of an ambient noise application, we show three ex-
 242 amples of Horizontal-to-Vertical Spectral Ratio (HVSR) (Nakamura, 1989; Molnar et al.,
 243 2022) surveys in Brussels, Belgium. In the framework of a shallow geothermal feasibil-
 244 ity study, we prospected several sites in Brussels with non-invasive ambient noise obser-
 245 vations prior to drilling. For the region of Brussels (Belgium), a conversion law exists
 246 to estimate the depth to bedrock from fundamental resonance frequency (f_0) values, de-
 247 rived from Horizontal-to-Vertical Spectral Ratio (HVSR) analysis of ambient noise mea-
 248 surements co-located with well logs (Van Noten et al., 2022). In the Brussels capital re-
 249 gion, the main acoustic impedance contrast corresponds to a fundamental frequency range
 250 between 0.6 and 1.6 Hz (Van Noten et al., 2022).

251 At first, the data of the ideal case-study of the instrument comparison test (fig. 3)
 252 have been analyzed using Geopsy (Wathelet et al., 2020). The location of the perma-
 253 nent station (BE.UCCS) within the cave of the Royal Observatory of Belgium (ROB)
 254 reassures constant environmental conditions (e.g., stable temperature, no insulation). The
 255 circular street present around the ROB also provides sufficient distance and azimuthal
 256 coverage of anthropogenic noise sources. In this case study, the same time windows (120s
 257 long) have been used for all co-located instruments and the horizontal components have
 258 been averaged when computing the HVSR spectra. The HVSR spectra for all instruments
 259 (fig. 6a) are congruent for the most parts. The fundamental frequency f_0 can be repro-
 260 duced by all sensors within 50% of the given uncertainty range (given as one standard
 261 deviation in Geopsy). For the HVSR amplitude at the f_0 , the Lennartz seismometer (con-
 262 nected to the City-shark) is comparable to the UCCS, Güralp permanent sensor. The
 263 node on the tripod gives a 10% higher and the node in the bucket a 15% lower ampli-
 264 tude value. For frequencies above 13 Hz, the HVSR curve computed from the nodal in-
 265 strument in the bucket deviates strongly and contains a second peak at 27.5 Hz. We pre-
 266 sume this peak is related either to a bad coupling of the spike base in the sand-filled bucket,
 267 or to an impedance contrast between the bucket and the tiling floor with its concrete base.
 268 Considering the lower HVSR amplitude at f_0 , the former is more likely as tilting shows
 269 stronger negative effects of the horizontal than the vertical components according to the
 270 manufacturer.

271 Under real-world conditions we present two examples from the southern part of Brus-
 272 sels. At the first location (fig. 6b), located next to the former *Brasserie Wielemans*, the
 273 Lennartz 5s with Cityshark and a SmartSolo node with a tripod base have been placed

274 on a sidewalk, 10 cm apart. The street presents high traffic amounts, including public
 275 busses, streetcars and pedestrians passing next to the sensors. The second location, lo-
 276 cated 200m away from the first case (*Wiels Cultural Center*, fig. 6c) consists of a park-
 277 ing spot next to the same street and a community garden. That allowed us to install the
 278 Lennartz and tripod node next to a node with a spike for comparison. Distances between
 279 the sensors lie between 5 and 10 m. The f_0 values obtained at both locations are the same
 280 on average and given the uncertainties. This is expected as both locations show no el-
 281 evation difference and have a similar geologic subsurface structure located in the Senne-
 282 valley. Above 1.3 Hz the HVSR curves for each location are congruent. The shape of the
 283 HV peak for the *Brasserie Wielemans* is sharper and presents smaller uncertainties. The
 284 *Wiels* location demonstrates larger variations in f_0 as well as the corresponding ampli-
 285 tude.

286 The HVSR curves deviate strongly for frequencies below their f_0 peaks. The in-
 287 spection of all analyzed time windows for the spectral analysis in Geopsy reveals much
 288 stronger fluctuation of the individual HVSR curves below 0.8 Hz. This leads to the wider
 289 average HVSR peak around f_0 in this frequency range. Below the S-wave resonance fre-
 290 quency the wavefield is dominated by body-waves and nearby sources (Lunedei & Malis-
 291 chewsky, 2015). In a densed urban area, as shown in the two examples, it might be im-
 292 possible to decouple the instrument from the noise generating infrastructure (i.e., side-
 293 walk of a heavily used street). In addition, noise-receiver distances are short and noise
 294 sources are non-stationary. Here, we recommend careful selection of investigation sites
 295 with longer recording periods and multiple locations. The impact of the noise instabil-
 296 ity below 0.8 Hz could be reduced through restitution of the raw waveform data. This
 297 step limits the amplitude differences of the mean HVSR curves as presented in figure 6.

298 The main distinction between the SmartSolo nodes and the classical seismometer-
 299 digitizer set-up became obvious in the handling of the hardware during the survey. The
 300 integrated node sensors outperform classical instruments in size, weight and usability.
 301 In the same time needed for one trained surveyor to install a seismometer-digitizer set-
 302 up, a single surveyor can transport and install up to 4 nodes. The use of multiple instru-
 303 ments might introduce some redundancy, but allows to capture potential lateral varia-
 304 tions over short distances. Especially in urban contexts, additional sensors assure suc-
 305 cessful data recordings in cases of unwanted noise sources (e.g., traffic, pumps, etc.), un-
 306 known subsurface cavities (e.g., channels, sewers) or bad coupling (see above).

307 **Conclusions**

308 With three different “lab-based” tests using coherent ground motion recordings,
309 we demonstrated the high performance of the 3C SmartSolo sensors (IGU-16HR-3C).
310 The manufacturer given values for the transfer function could be reproduced in the so-
311 called huddle-test and were used to accurately reconstitute the instrument responses. Their
312 overall self-noise resides around the global minimum noise level (Peterson, 1993) over a
313 wide frequency range, through which they become versatile and useful for a wide range
314 of seismological applications, such as seismotectonics in local and regional distances, noise
315 tomography, ambient noise studies and applied geophysics. In direct comparison to stan-
316 dard instruments in use for decades for seismological surveys, the nodes show at least
317 the same performance levels, even beyond their natural frequency, while having the ad-
318 vantage of highly reduced purchasing costs, weight, and installation and dismantling time.
319 This study endorses the use of SmartSolo nodes as low-budget alternatives, either for
320 Large N installations or for research groups that have limited financial resources to per-
321 form seismotectonic or ambient noise studies using more expensive but higher-quality
322 seismic sensors.

323 **Data and Resources**

324 All seismic waveforms processed for this study have been obtained at the Royal Obser-
325 vatory of Belgium and are available alongside with the publicly available python codes
326 at <https://gitlab-as.oma.be/martinz/smartsolo-nodes-paper>.

327 **Declaration of Competing Interests**

328 The authors declare no competing interests.

329 **Acknowledgments**

330 The authors want to thank the staff of the Seismology-Gravimetry section at the
331 Royal Observatory of Belgium for constructive discussions during various steps of the
332 study. A special thanks goes to Giovanni Rapagnani for his help in data analysis and
333 reviewing the manuscript. MZ has been funded by two projects of the Belgian Science
334 Policy Office (BELSPO) including (1) the Belgian contribution to EPOS (FSIRI/33/EP1)
335 and (2) the BRAIN-be 2.0 GeoCamb project (B2/191/P1/GEOCAMB).

References

- 336
- 337 Ahrens, J., Hendrickson, B., Long, G., Miller, S., Ross, R., & Williams, D. (2011).
 338 Data-intensive science in the us doe: case studies and future challenges. *Comput-*
 339 *ing in Science & Engineering*, 13(6), 14–24.
- 340 Anthony, R. E., Ringler, A. T., Wilson, D. C., & Wolin, E. (2019). Do low-cost
 341 seismographs perform well enough for your network? an overview of laboratory
 342 tests and field observations of the osop raspberry shake 4d. *Seismological Research*
 343 *Letters*, 90(1), 219–228.
- 344 Arrowsmith, S., Trugman, D., MacCarthy, J., Bergen, K., Lumley, D., & Magnani,
 345 M. (2022). Big data seismology. *Reviews of Geophysics*, 60(2), e2021RG000769.
- 346 Bergen, K. J., Chen, T., & Li, Z. (2019). Preface to the focus section on machine
 347 learning in seismology. *Seismological Research Letters*, 90(2A), 477–480.
- 348 Bozdag, E., Lefebvre, M., Lei, W., Peter, D., Smith, J., Komatitsch, D., & Tromp,
 349 J. (2014). Big data and high-performance computing in global seismology. In *Egu*
 350 *general assembly conference abstracts* (p. 16606).
- 351 Brenguier, F., Kowalski, P., Ackerley, N., Nakata, N., Boué, P., Campillo, M., ...
 352 Chaput, J. (2015, 11). Toward 4D Noise-Based Seismic Probing of Volcanoes:
 353 Perspectives from a Large-N Experiment on Piton de la Fournaise Volcano. *Seis-*
 354 *mological Research Letters*, 87(1), 15-25. doi: 10.1785/0220150173
- 355 Calais, E., Symithe, S., Monfret, T., Delouis, B., Lomax, A., Courboulex, F., ...
 356 others (2022). Citizen seismology helps decipher the 2021 haiti earthquake.
 357 *Science*, 376(6590), 283–287.
- 358 Castellanos, J. C., & Clayton, R. W. (2021). The fine-scale structure of long beach,
 359 california, and its impact on ground motion acceleration. *Journal of Geophysical*
 360 *Research: Solid Earth*, 126(12), e2021JB022462.
- 361 Chatelain, J.-L., Gueguen, P., Guillier, B., Frechet, J., Bondoux, F., Sarrault, J.,
 362 ... Neuville, J.-M. (2000). Cityshark: A user-friendly instrument dedicated
 363 to ambient noise (microtremor) recording for site and building response studies.
 364 *Seismological Research Letters*, 71(6), 698–703.
- 365 Chen, K. H., Bossu, R., & Liang, W.-T. (2020). *The power of citizen seismology:*
 366 *Science and social impacts* (Vol. 8). Frontiers Media SA.
- 367 Chmiel, M., Mordret, A., Boué, P., Brenguier, F., Lecocq, T., Courbis, R., ...
 368 Van der Veen, W. (2019, 05). Ambient noise multimode Rayleigh and Love

- 369 wave tomography to determine the shear velocity structure above the Groningen
 370 gas field. *Geophysical Journal International*, 218(3), 1781-1795. Retrieved from
 371 <https://doi.org/10.1093/gji/ggz237> doi: 10.1093/gji/ggz237
- 372 Dean, T., & Sweeney, D. (2019). Recent advances in nodal land seismic acquisition
 373 systems. *ASEG Extended Abstracts*, 2019(1), 1-4.
- 374 Dean, T., Tulett, J., & Barnwell, R. (2018). Nodal land seismic acquisition: The
 375 next generation [Journal Article]. *First Break*, 36(1), 47-52. doi: [https://doi.org/](https://doi.org/10.3997/1365-2397.n0061)
 376 [10.3997/1365-2397.n0061](https://doi.org/10.3997/1365-2397.n0061)
- 377 De Plaen, R. S., Márquez-Ramírez, V. H., Pérez-Campos, X., Zuñiga, F. R.,
 378 Rodríguez-Pérez, Q., Gómez González, J. M., & Capra, L. (2021). Seismic
 379 signature of the covid-19 lockdown at the city scale: a case study with low-cost
 380 seismometers in the city of querétaro, mexico. *Solid Earth*, 12(3), 713-724.
- 381 GEOFON Data Centre. (1993). *Geofon seismic network*. Deutsches Geo-
 382 Forschungszentrum GFZ. Retrieved from [http://geofon.gfz-potsdam.de/](http://geofon.gfz-potsdam.de/doi/network/GE)
 383 [doi/network/GE](http://geofon.gfz-potsdam.de/doi/network/GE) doi: 10.14470/TR560404
- 384 Hand, E. (2014). *A boom in boomless seismology*. American Association for the Ad-
 385 vancement of Science.
- 386 Havskov, J., & Alguacil, G. (2015). *Instrumentation in earthquake seismology*.
 387 Springer. (Publication Title: Instrumentation in Earthquake Seismology) doi:
 388 [10.1007/978-3-319-21314-9](https://doi.org/10.1007/978-3-319-21314-9)
- 389 Karplus, M., & Schmandt, B. (2018). Preface to the focus section on geophone array
 390 seismology. *Seismological Research Letters*, 89(5), 1597-1600.
- 391 Kong, Q., Trugman, D. T., Ross, Z. E., Bianco, M. J., Meade, B. J., & Gerstoft, P.
 392 (2019). Machine learning in seismology: Turning data into insights. *Seismological*
 393 *Research Letters*, 90(1), 3-14.
- 394 Lecocq, T., Hicks, S. P., Van Noten, K., Van Wijk, K., Koelemeijer, P., De Plaen,
 395 R. S., ... others (2020). Global quieting of high-frequency seismic noise due to
 396 covid-19 pandemic lockdown measures. *Science*, 369(6509), 1338-1343.
- 397 Lunedei, E., & Malischewsky, P. (2015). A review and some new issues on the the-
 398 ory of the h/v technique for ambient vibrations. *Perspectives on European earth-*
 399 *quake engineering and seismology*, 371-394.
- 400 MacCarthy, J., Marciello, O., & Trabant, C. (2020). Seismology in the cloud: A new
 401 streaming workflow. *Seismological Research Letters*, 91(3), 1804-1812.

- 402 Molnar, S., Sirohey, A., Assaf, J., Bard, P.-Y., Castellaro, S., Cornou, C., . . . others
 403 (2022). A review of the microtremor horizontal-to-vertical spectral ratio (mhvsr)
 404 method. *Journal of Seismology*, 1–33.
- 405 Nakamura, Y. (1989). A method for dynamic characteristics estimation of subsur-
 406 face using microtremor on the ground surface. *Railway Technical Research Insti-
 407 tute, Quarterly Reports*, 30(1).
- 408 Obermann, A., Sánchez-Pastor, P., Wu, S., Wollin, C., Baird, A. F., Isken, M. P.,
 409 . . . Wiemer, S. (2022, July). Combined Large-N Seismic Arrays and DAS Fiber
 410 Optic Cables across the Hengill Geothermal Field, Iceland. *Seismological Research
 411 Letters*. Retrieved 2022-08-17, from <https://doi.org/10.1785/0220220073> doi:
 412 10.1785/0220220073
- 413 Peterson, J. R. (1993). *Observations and modeling of seismic background noise*
 414 (Tech. Rep.). US Geological Survey. doi: 10.3133/ofr93322
- 415 Quinteros, J., Carter, J. A., Schaeffer, J., Trabant, C., & Pedersen, H. A. (2021).
 416 Exploring approaches for large data in seismology: User and data repository per-
 417 spectives. *Seismological Research Letters*, 92(3), 1531–1540.
- 418 Ringler, A., Hutt, C., Evans, J., & Sandoval, L. (2011). A comparison of seismic in-
 419 strument noise coherence analysis techniques. *Bulletin of the Seismological society
 420 of America*, 101(2), 558–567.
- 421 Ringler, A. T., Anthony, R. E., Karplus, M., Holland, A., & Wilson, D. C. (2018).
 422 Laboratory tests of three z-land fairfield nodal 5-hz, three-component sensors.
 423 *Seismological Research Letters*, 89(5), 1601–1608.
- 424 Ringler, A. T., Sleeman, R., Hutt, C. R., & Gee, L. S. (2014). Seismometer self-
 425 noise and measuring methods. In *Encyclopedia of earthquake engineering* (pp. 1–
 426 13). Springer Berlin Heidelberg. doi: 10.1007/978-3-642-36197-5_175-1
- 427 Roux, P., Bindi, D., Boxberger, T., Colombi, A., Cotton, F., Douste-Bacque, I., . . .
 428 Pondaven, I. (2018, 01). Toward Seismic Metamaterials: The METAFORÉT
 429 Project. *Seismological Research Letters*, 89(2A), 582-593. doi: 10.1785/
 430 0220170196
- 431 Royal Observatory of Belgium. (1985). *Belgian seismic network*. International Fed-
 432 eration of Digital Seismograph Networks. Retrieved from [https://www.fdsn.org/
 433 networks/detail/BE/](https://www.fdsn.org/networks/detail/BE/) doi: 10.7914/SN/BE
- 434 Scherbaum, F. (2006). *Of poles and zeros: Fundamentals of digital seismology*

- 435 (Vol. 15). Springer Science & Business Media.
- 436 Sleeman, R., Van Wettum, A., & Trampert, J. (2006). Three-channel correlation
437 analysis: A new technique to measure instrumental noise of digitizers and seismic
438 sensors. *Bulletin of the Seismological Society of America*, *96*(1), 258–271.
- 439 Subedi, S., Hetényi, G., Denton, P., & Sauron, A. (2020). Seismology at school
440 in nepal: a program for educational and citizen seismology through a low-cost
441 seismic network. *Frontiers in Earth Science*, *73*.
- 442 Van Noten, K., Lecocq, T., Goffin, C., Meyvis, B., Molron, J., Debacker, T. N., &
443 Devleeschouwer, X. (2022). Brussels' bedrock paleorelief from borehole-controlled
444 power laws linking polarised h/v resonance frequencies and sediment thickness.
445 *Journal of Seismology*, *26*(1), 35–55.
- 446 Wathelet, M., Chatelain, J.-L., Cornou, C., Giulio, G. D., Guillier, B., Ohrnberger,
447 M., & Savvaidis, A. (2020). Geopsy: A user-friendly open-source tool set for
448 ambient vibration processing. *Seismological Research Letters*, *91*(3), 1878–1889.

449 **Full mailing address for each author**

450 Martin Zeckra - martin.zeckra@seismology.be

451 Koen Van Noten - koen.vannoten@seismology.be

452 Thomas Lecocq - thomas.lecocq@seismology.be